

An adaptive non-conforming finite-element method for Reissner–Mindlin plates

Carsten Carstensen^{1,†} and Kerstin Weinberg^{2,*‡}

¹*Institute for Applied Mathematics and Numerical Analysis, Vienna University of Technology,
Wiedner Hauptstrasse 8-10/115, A-1040 Wien, Austria*

²*Graduate Aeronautical Laboratories, California Institute of Technology, Pasadena, CA 91125, U.S.A.*

SUMMARY

Adaptive algorithms are important tools for efficient finite-element mesh design. In this paper, an error controlled adaptive mesh-refining algorithm is proposed for a non-conforming low-order finite-element method for the Reissner–Mindlin plate model. The algorithm is controlled by a reliable and efficient residual-based *a posteriori* error estimate, which is robust with respect to the plate's thickness. Numerical evidence for this and the efficiency of the new algorithm is provided in the sense that non-optimal convergence rates are optimally improved in our numerical experiments. Copyright © 2003 John Wiley & Sons, Ltd.

KEY WORDS: Reissner–Mindlin plate; *a posteriori* error estimates; adaptive algorithm; mixed finite-element method; non-conforming finite-element method

1. INTRODUCTION

The Reissner–Mindlin model of the plate bending problem concerns the transversal displacement w and the rotations of the plate normal $\phi = (\phi_i)_{i=1,2}$ and reads in its weak form: Given $f \in L^2(\Omega)$ find $(\phi, w) \in H_0^1(\Omega)^2 \times H_0^1(\Omega)$ such that, for all $(\psi, \mu) \in H_0^1(\Omega)^2 \times H_0^1(\Omega)$,

$$(\varepsilon(\phi); \mathbb{C}\varepsilon(\psi)) + t^{-2}(\phi - \nabla w; \psi - \nabla \mu) = (f; \mu) \quad (1)$$

Here $(\cdot; \cdot)$ is the scalar product in $L^2(\Omega)$, $\varepsilon(\phi)$ is the symmetric part of the gradient $\nabla \phi$ and \mathbb{C} is the elasticity tensor; detailed notation will be given in Section 2. A straightforward discretization of Equation (1) by a finite-element method may deteriorate as the plate thickness t becomes small. This is well known as the shear locking phenomenon.

*Correspondence to: Kerstin Weinberg, Graduate Aeronautical Laboratories, California Institute of Technology, Pasadena, CA 91125, U.S.A.

†E-mail: carsten.carstensen@tuwien.ac.at

‡E-mail: weinberg@aero.caltech.edu

Contract/grant sponsor: German Research Foundation (DFG)

*Received 6 July 2001
Revised 7 October 2001
Accepted 3 July 2002*

Arnold and Falk analysed in Reference [1] a simplified version of Equation (1). They involved conforming and non-conforming low-order finite-element spaces and an L^2 -projection onto piecewise constants in their locking-free finite-element discretization [1], cf. Section 2. An *a posteriori* error estimate for the simplified problem, with residuals $\tilde{\eta}_T$ for every element T of the triangulation and of edge jumps $\tilde{\eta}_E$ for an edge E , is shown to be reliable and efficient in Reference [2].

In this paper, we extend the theoretical results of References [1, 2] to the Reissner–Mindlin problem (Equation (1)) with non-homogeneous boundary conditions, non-smooth load functions f and/or non-smooth geometry. We introduce a new adaptive mesh-refining algorithm for the simple and locking-free finite-element method for the Reissner–Mindlin plate model. Numerical evidence for the efficiency of the error controlled algorithm is provided by typical examples; non-optimal convergence rates are improved optimally.

The paper is organized as follows. The precise model and non-conforming low-order finite-element method will be described in Section 2. The discrete problem can be decoupled further for theoretical purposes via a discrete Helmholtz decomposition [1]. This and the generalized error estimator $\tilde{\eta}$ for the error e will be presented in Section 3. Section 4 describes the adaptive algorithm proposed. The robustness of the estimate is empirically verified in Section 5 where η/e stays bounded no matter in which way the mesh size or the thickness tends to zero. Section 6 concerns an example with a free (i.e. non-supported) boundary to study the performance of the adaptive algorithm for boundary layers. A sheet metal with hole and concentrated forces is discussed in Section 7. An example with a corner singularity on the L -shaped domain in Section 8 concludes our set of numerical examples. The exact solution is unknown and, owing to the non-conformity, the error cannot be extrapolated as in Reference [3]. The equivalent error estimator, however, illustrates the improved approximation of the adapted mesh refinement over the uniform refinements in all examples. The proof of reliability is based on arguments in Reference [2] for the simplified model of Equation (1). An outline and necessary modifications of the mathematical analysis conclude the paper in Section 9.

The main achievement of the adaptive algorithm and the *a posteriori* error control of this paper over other attempts [4] or purely heuristic approaches is the guaranteed robustness in the thickness t .

2. NOTATION AND FINITE-ELEMENT DISCRETIZATION

Assuming isotropic, linear elastic material behaviour the (scaled) elasticity operator \mathbb{C} in Equation (1) is defined by

$$\mathbb{C}\tau = \frac{1}{6k} \left[\tau + \frac{\nu}{1-\nu} \text{tr}(\tau)\mathbf{I} \right] \quad (2)$$

where $\text{tr}(\tau)$ is the trace of $\tau \in \mathbb{R}^{2 \times 2}$, \mathbf{I} is the 2×2 identity matrix, ν is the Poisson ratio, and $k = \frac{5}{6}$ is Reissner's shear correction factor. Moreover, $\varepsilon(\phi)$ denotes the symmetric gradient (the linear Green strain) $\varepsilon(\phi) := \text{sym} D\phi = (\frac{1}{2}(\partial\phi_j/\partial x_k + \partial\phi_k/\partial x_j))_{j,k=1,2}$ and ∇ is the gradient of a scalar function. With an additional shear term ζ ,

$$\zeta := t^{-2}(\nabla w - \phi) \quad (3)$$

and bilinear and linear forms (where $\phi_1, \phi_2, \psi_1, \psi_2, w \in H_D^1(\Omega)$ and $\zeta, \xi \in L^2(\Omega)$)

$$a(\phi; \psi) := \int_{\Omega} \varepsilon(\phi) : \mathbb{C} \varepsilon(\psi) \, dx \tag{4}$$

$$b(\psi, \mu; \zeta) := \int_{\Omega} (\nabla \mu - \psi) \zeta \, dx \tag{5}$$

$$c(\zeta; \xi) := \int_{\Omega} t^2 \zeta \xi \, dx \tag{6}$$

$$F(\phi, w) := \int_{\Omega} (f_{\phi} \phi + f_w w) \, dx + \int_{\Gamma_N} (g_{\phi} \phi + g_w w) \, ds \tag{7}$$

the *Continuous Problem* of the Reissner–Mindlin plate model is rewritten in a mixed formulation: Find $(\phi, w, \zeta) \in H_D^1(\Omega)^2 \times H_D^1(\Omega) \times L^2(\Omega)^2$ that satisfies, for all $(\psi, \mu, \xi) \in H_D^1(\Omega)^2 \times H_D^1(\Omega) \times L^2(\Omega)^2$,

$$a(\phi; \psi) + b(\psi, \mu; \zeta) = F(\psi, \mu) \tag{8}$$

$$b(\phi, w; \xi) + c(\zeta; \xi) = 0 \tag{9}$$

Here, $L^2(\Omega)$ and $H^1(\Omega)$ denote the usual Lebesgue and Sobolev spaces [5] and $H_D^1(\Omega)$ is the subspace of all functions with prescribed homogeneous boundary values at Γ_D . On the boundary Γ_N (with $\Gamma_D \cup \Gamma_N = \partial\Omega$, $\Gamma_D \cap \Gamma_N = \emptyset$), forces and moments $g := (g_w, g_{\phi})$ in $L^2(\Gamma_N)^3$ may apply as well as forces and moments within the domain $f := (f_w, f_{\phi}) \in L^2(\Omega)^3$; g and f are already scaled by a factor $Ekt^3/(2(1 + \nu))$, where E is the Young’s modulus.

Let \mathcal{T} be a regular triangulation of the bounded Lipschitz domain $\Omega \subseteq \mathbb{R}^2$ with polygonal boundary Γ into triangles (i.e. the domain is covered exactly and there are no hanging nodes, cf. Reference [5]). The \mathcal{T} -piecewise affine and globally continuous functions are denoted as $\mathcal{S}^1(\mathcal{T})$ while $\mathcal{S}^{1,NC}(\mathcal{T})$ denotes the \mathcal{T} -piecewise affine functions which are continuous at the midpoints \mathcal{M} of edges $E \in \mathcal{E}$, $\mathcal{L}^0(\mathcal{T})$ denotes \mathcal{T} -piecewise constant functions with the L^2 -projection P_0 onto $\mathcal{L}^0(\mathcal{T})$. The corresponding modifications with given boundary values at Γ_D and $\mathcal{M} \cap \Gamma$, respectively, are written as $\mathcal{S}_D^1(\mathcal{T})$ and $\mathcal{S}_D^{1,NC}(\mathcal{T})$. The cubic bubble functions $b_T := \lambda_1 \lambda_2 \lambda_3 \in H_0^1(T)$, where λ_j denotes the barycentric co-ordinate of the vertex j on the triangle T , define $\mathcal{B}^3(\mathcal{T}) := \{f \in H_0^1(\Omega) : \forall T \in \mathcal{T}, f|_T = \mu_T b_T \text{ for some } \mu_T \in \mathbb{R}\}$.

The *Discrete Problem* reads: Find $(\phi_h, w_h, \zeta_h) \in \mathcal{H}_h := (\mathcal{S}_D^1(\mathcal{T}) \oplus \mathcal{B}^3(\mathcal{T}))^2 \times \mathcal{S}_D^{1,NC}(\mathcal{T}) \times \mathcal{S}^0(\mathcal{T})$ that satisfies, for all $(\psi_h, \mu_h, \xi_h) \in \mathcal{H}_h$,

$$a(\phi_h; \psi_h) + b_h(\psi_h, \mu_h; \zeta_h) = F(\psi_h, \mu_h) \tag{10}$$

$$b_h(\phi_h, w_h; \xi_h) - c(\zeta_h; \xi_h) = 0 \tag{11}$$

Here $b_h(\psi_h, \mu_h; \zeta_h) := \int_{\Omega} (\nabla_{\mathcal{T}} \mu_h - \psi_h) \zeta_h \, dx$ replaces b according to the non-conforming μ_h .

The applied boundary conditions do not cover the most general possible situation. First, the part Γ_D may be different for ϕ, ϕ_h and w, w_h , respectively. Hence $\Gamma_{D,\phi}$ and $\Gamma_{D,w}$ are required instead of Γ_D . Second, the boundary data may be inhomogeneous. The adaption of

the presented situation (which essentially covers all our numerical examples below) to more general problems is straightforward.

3. DECOMPOSED PROBLEM

Arnold and Falk employed a Helmholtz decomposition of the discrete shear term ζ_h [1],

$$\zeta_h := t^{-2}(\nabla_{\mathcal{T}} w_h - P_0 \phi_h) = \nabla_{\mathcal{T}} r_h + \text{Curl } p_h \tag{12}$$

to decompose the *Discrete Problem*: Find $(r_h, \phi_h, p_h, w_h) \in \mathcal{H}_s := \mathcal{S}_D^{1,NC}(\mathcal{T}) \times (\mathcal{S}_D^1(\mathcal{T}) \oplus \mathcal{B}^3(\mathcal{T}))^2 \times \mathcal{S}_N^1(\mathcal{T}) \times \mathcal{S}_D^{1,NC}(\mathcal{T})$ such that, for all $(s_h, \psi_h, q_h, \mu_h) \in \mathcal{H}_s$,

$$(\nabla_{\mathcal{T}} r_h; \nabla_{\mathcal{T}} \mu_h) = F(0, \mu_h) \tag{13}$$

$$(\varepsilon(\phi_h); \mathbb{C}\varepsilon(\psi_h)) - (\text{Curl } p_h + \nabla_{\mathcal{T}} r_h; \psi_h) = F(\psi_h, 0) \tag{14}$$

$$(\phi_h + t^2 \text{Curl } p_h; \text{Curl } q_h) = 0 \tag{15}$$

$$(\nabla_{\mathcal{T}} w_h - \phi_h - t^2 \nabla_{\mathcal{T}} r_h; \nabla_{\mathcal{T}} s_h) = 0 \tag{16}$$

Two differential operators curl are defined by $\text{Curl} := (-\partial/\partial x_2, \partial/\partial x_1)$ and $\text{rot } \psi := \partial\psi_1/\partial x_2 - \partial\psi_2/\partial x_1$, $\psi \in H^1(\Omega)^2$. The space $\mathcal{S}_N^1(\mathcal{T})$ equals $\mathcal{S}^1(\mathcal{T})/\mathbb{R}$ if $\Gamma_D = \partial\Omega$ and complements $\mathcal{S}_D^{1,NC}(\mathcal{T})$ by $\mathcal{S}_N^1(\mathcal{T}) := \{q_h \in \mathcal{S}^1(\mathcal{T}) : \partial q_h/\partial s = 0 \text{ on each } E \in \mathcal{E}_N\}$, \mathcal{E}_N denotes the set of edges on $\Gamma_N := \partial\Omega \setminus \Gamma_D$.

It is shown in Reference [1] that a simplified form of the decomposed discrete problem (13)–(16) has a unique solution. With an analogous strategy this can be shown for Equations (13)–(16) and for the equivalent discrete problem (10)–(11) as well. With a positive and $(h_{\mathcal{T}}, t, f, g)$ -independent constant C_1 , there holds the *a priori* error estimate

$$|\phi - \phi_h|_{1,2} + \|r - r_h\|_2 + \|\nabla r - \nabla_{\mathcal{T}} r_h\|_2 + \|\nabla w - \nabla_{\mathcal{T}} w_h\|_2 + \|p - p_h\|_2 + t|p - p_h|_{1,2} \leq C_1 h_{\mathcal{T}} \|f\|_2 \tag{17}$$

where $\|\cdot\|_2$ and $|\cdot|_{1,2}$ are the $L^2(\Omega)$ -norm and the $H^1(\Omega)$ -seminorm, respectively, and the polygonal domain Ω is convex. In Reference [2] an *a posteriori* error estimate $\tilde{\eta}^2$ of a simplified version of (13)–(16) is established as the square root of the sum of all element contributions $\tilde{\eta}_T^2$,

$$\tilde{\eta}_T^2 := \int_T |\phi_h - P_0 \phi_h|^2 dx + h_T^2 \int_T |\zeta_h + \Delta \phi_h|^2 dx + \min \left\{ 1, \left(\frac{h_T}{t} \right)^2 \right\} \int_T |\text{rot } \phi_h|^2 dx$$

and of all edge contributions $\tilde{\eta}_E^2$

$$\tilde{\eta}_E^2 := h_E \int_{E \cap \Gamma} |[D(\phi_h)]n_E|^2 ds + \min\{t^3, t^2 h_E\} \int_E |[\zeta_h]t_E|^2 ds \tag{18}$$

with gradient D ; t is here a parameter with $0 < t < 1$. The *a posteriori* error estimate $\tilde{\eta} := (\sum_{T \in \mathcal{T}} \tilde{\eta}_T^2 + \sum_{E \in \mathcal{E}} \tilde{\eta}_E^2)^{1/2}$ is reliable and efficient (cf. Reference [2]), i.e. it is a lower and upper bound of the error

$$e_N := |\phi - \phi_h|_{1,2} + \|\nabla w - \nabla_{\mathcal{T}} w_h\|_2 + t|p - p_h|_{1,2} + \|p - p_h\|_2 \tag{19}$$

The positive constants C_2 and C_3 in the efficiency and reliability estimate

$$C_2 \eta - \text{h.o.t.} \leq e_N \leq C_3 \eta + \text{h.o.t.} \tag{20}$$

are uniform in $0 < t < 1$, and h_T and h_E depend only on the minimal interior angle in the triangulation \mathcal{T} and on Ω . The higher-order terms (h.o.t.) in the upper and lower bound, respectively, are terms of r_h . The lower bound in (20) holds in a local (elementwise resp. patchwise) form up to known higher-order terms such as $(t + h_T)h_T(\int_T |f_w|^2 dx)^{1/2}$. Note, that the additional terms p resp. r and their discrete counterparts p_h resp. r_h in (20) do *not* appear in the solution of the Reissner–Mindlin plate model (1).

4. THE ADAPTIVE FINITE-ELEMENT SCHEME

The discrete problem (13)–(16) is of particular interest because its decomposed form is necessary for the mathematical analysis only. In the numerical implementation the additional variables r_h and p_h may be avoided. With the discrete shear term (12) we will deduce an *a posteriori* error estimate for the solution of (10)–(11) in Theorem 9.1. This error estimate η can be computed elementwise,

$$\eta := \left(\sum_{T \in \mathcal{T}} \eta_T^2 \right)^{1/2} \tag{21}$$

from local error contributions

$$\begin{aligned} \eta_T^2 := & \int_T |\phi_h - \nabla w_h + t^2 \zeta_h|^2 dx + h_T^2 \int_T |f_\phi + \text{div } \mathbb{C}\varepsilon(\phi_h) + \zeta_h|^2 dx + \min\{1, (h_T/t)^2\} \int_T |\text{rot } \phi_h|^2 dx \\ & + \sum_{E \subset \partial T} \left(h_E \int_{E \setminus \Gamma_b} |[\mathbb{C}\varepsilon(\phi_h)]n_E|^2 ds + \min\{t^3, t^2 h_E\} \int_E |[\zeta_h]t_E|^2 ds \right) \end{aligned} \tag{22}$$

for an element T of length $h_T := \text{diam}(T)$ with edges E of length $h_E := \text{diam}(E)$ and with jumps $[\cdot]$ across and edge E and normal and tangential unit vectors n_E and t_E .

The numerical validation of efficiency and reliability of error estimator (21) is presented in Section 5 for the solution error (19) as well as for the error in natural energy norm. A mathematical analysis based on Reference [2] is sketched in Section 9. Moreover, we regard the elementwise contributions (22) as refinement indicators in our adaptive mesh-refining algorithm.

Adaptive Algorithm (A)

- (a) Start with coarse mesh \mathcal{T}_0 .
- (b) Solve discrete problem with respect to \mathcal{T}_k with N degrees of freedom.



Figure 1. Red–green–blue refinements of a triangle.

- (c) Compute η_T for all $T \in \mathcal{T}_k$.
- (d) Compute error bound $\eta_N := (\sum_{T \in \mathcal{T}_k} \eta_T^2)^{1/2}$ and terminate or go to (e).
- (e) Mark element T iff $\eta_T \geq \frac{1}{2} \max_{T' \in \mathcal{T}_k} \eta_{T'}$.
- (f) Refine marked elements, generate new mesh \mathcal{T}_{k+1} and go to (b) with updated k .

We employ red–green–blue refining procedures [6]. Red-refining means to bisect the sides of one marked triangle and re-mesh with four congruent triangles (first picture of Figure 1). To avoid hanging nodes, further refinements of neighbouring elements are possibly performed according to one of the choices in Figure 1. In any case, one longest side is divided. In this way we avoid hanging nodes as well as degenerated elements.

5. NUMERICAL VALIDATION

Since the solution of Reissner–Mindlin model (1) tends to the solution of Kirchhoff’s theory when $t \rightarrow 0$, we compare the results of error estimate (21) with the true error for the (different) reference solution

$$w(x, y) = (x^2 - 1/4)^2 (y^2 - 1/4)^2 \quad \text{for } (x, y) \in \Omega := (-1/2, +1/2)^2 \quad (23)$$

with $f_w = Et^3/(12(1 - \nu^2))\Delta\Delta w$, $E = 10.92$ MPa, $\nu = 0.3$ and thickness $t = 0.001$ m.

By symmetry we calculated only one quarter $[0, 0.5]^2$ m of the domain Ω with an initial mesh \mathcal{T}_0 of two triangles with $N = 11$ degrees of freedom. Figure 2 displays the convergence of error estimate η_N (21) with uniformly refined meshes (stars). Here and below the error terms and their estimates η_N from (21) are plotted versus the number of degrees of freedom N in a log/log-scale. Owing to $N \propto h^{-2}$ in two dimensions, a slope $-\frac{1}{2}$ in the figures corresponds to an experimental convergence rate 1.

To measure the error we compute the H^1 -seminorm and L^2 -norm of the difference between Kirchhoff’s and the finite-element solution for the rotation vector $|\phi - \phi_h|_{1,2}$ with $\phi = \nabla w$ and for the displacement gradient $\|\nabla w - \nabla_{\mathcal{T}} w_h\|_2$, respectively. The error norm (19) is not directly computable because the error contribution $p - p_h$ does not appear in (1) and (10)–(11).

To approximate $e \approx e_N$ we proceed as follows. With w from Equation (23) and $\phi = \nabla w$ (for the reference solution) we have $\zeta = 0$ and so $p = 0$, $r = 0$. To compute p_h we recast (12) multiplied with $\text{Curl } \phi_h \in \mathcal{S}_D^1(\mathcal{T})$ into

$$(\nabla p_h; \nabla \phi_h) = t^{-2} (\text{rot } \phi_h; \phi_h) \quad (24)$$

where we used $(\text{Curl } \phi_h, P_0 \phi_h) = (\text{Curl } \phi_h; \phi_h) = (\text{rot } \phi_h; \phi_h)$ with integration by parts. By solving the Laplace problem (24) we determine p_h (ϕ_h is part of the computed finite-element solution). Then,

$$t|p - p_h|_{1,2} = t^{-1} (\text{rot } \phi_h; p_h) \quad \text{and} \quad \|p - p_h\|_2 = \|p_h\|_2 \quad (25)$$

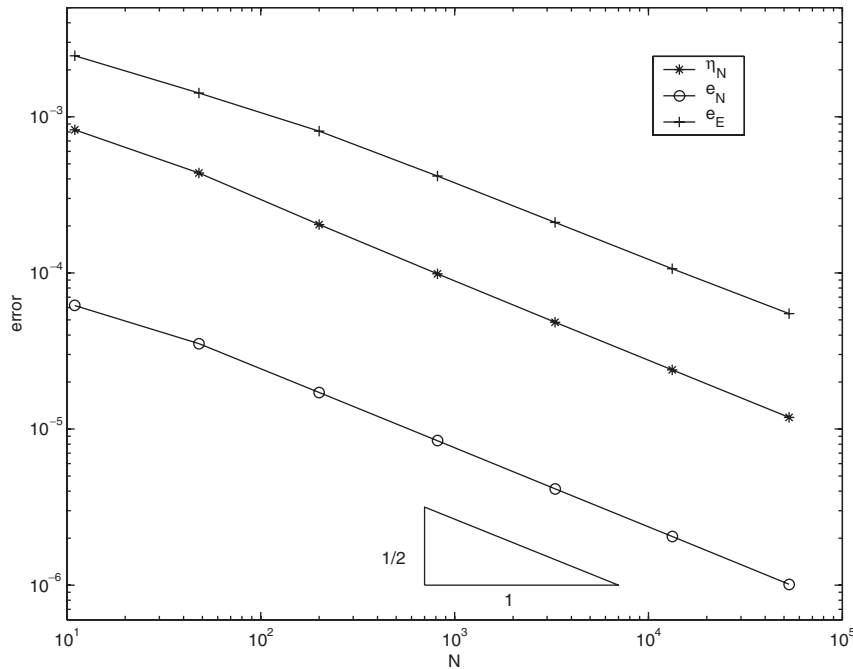


Figure 2. Exact error and error estimate in the example of Section 5 with analytical solution Equation (23).

In this way, (19) is approximated by the computable reference quantity

$$e_N := |\nabla w - \phi_h|_{1,2} + \|\nabla w - \nabla_{\mathcal{F}} w_h\|_2 + t^{-1}(\text{rot } \phi_h; p_h) + \|p_h\|_2 \approx e \tag{26}$$

and displayed in Figure 2 (circles) as a function of the number N of the degrees of freedom.

Additionally, we monitor the error convergence in natural energy norm (marked by + in Figure 2) which is approximated by

$$e_E^2 := \|\mathbb{C}^{1/2} \varepsilon(\nabla w - \phi_h)\|^2 + t^{-2} \|\phi_h - \nabla_{\mathcal{F}} w_h\|^2 \tag{27}$$

In Figure 2, the convergence of all error contributions is optimal with convergence rate 1. The *a posteriori* error estimate η_N obviously converges with identical rate as the true solution error, that it is (up to a constant) a bound of error (26) resp. (19) and (27).

Table I displays the values of error estimate η_N divided by solution error e_N (26) computed for uniformly refined plates of different thickness t . We observe almost constant estimate to error ratios. That the asymptotic exactness (efficiency and reliability) is confirmed as in Figure 2 (read Table I line by line for uniform mesh refining). The estimate η_N appears also to be robust, i.e. it does *not* depend on the plate thickness (read Table I column by column for falling thickness). Estimate (21) appears very accurate in the sense that the true and the indicated convergence rates coincide.

In conclusion, Table I provides numerical evidence for our theoretical results of Section 9. It strongly supports that η_N/e_N is bounded from above and below (t, N) -independently.

Table I. Error estimate η_N divided by error e_N for varying thickness in the example of Section 5.

η_N/e_N	\mathcal{T}_2 $N=200$	\mathcal{T}_3 $N=816$	\mathcal{T}_4 $N=3296$	\mathcal{T}_5 $N=13248$	\mathcal{T}_6 $N=58120$
$t=10^{-2}$	11.8501	11.7278	11.9273	11.9814	11.8388
$t=10^{-3}$	11.9023	11.7229	11.6782	11.6748	11.7192
$t=10^{-4}$	11.9110	11.7375	11.6986	11.6873	11.7330

6. PLATE WITH FREE BOUNDARY

The exact solution of the Reissner–Mindlin plate model (1) typically exhibits edge effects. More precisely, depending on boundary conditions and geometry the derivatives of the normal-rotation vector $\phi = (\phi_i)_{i=1,2}$ may vary rapidly in a narrow layer around the boundary. Boundary layers are weak in the case of clamped plates $(\phi, w) \in H_0^1(\Omega)^2 \times H_0^1(\Omega)$, where discretization (10)–(11) as well as error estimate (21) were analysed for, but they are relatively strong for free, i.e. not supported, boundaries. Therefore, we investigate here numerically whether our error estimate (21) measures the error due to boundary effects in an appropriate way.

Edge effects can be analysed by substituting the unknown rotations of the plate normal ϕ with a new variable $\text{rot}(\phi) \in L^2(\Omega)$, $\text{rot}(\phi) = \partial\phi_1/\partial x_2 - \partial\phi_2/\partial x_1$. In this way, the Reissner–Mindlin equations decouple into a boundary-layer equation for $\text{rot}(\phi)$ and an interior equation for the transversal displacement w (cf. Reference [7] for details and further references). In a simple model problem with known analytical solution for the boundary layer equation (obtained as in Reference [7] by series expansion) we monitor here edge effects on a free curved boundary. We consider a quarter of a circular plate with radius $r=1$ m and plate thickness $t=0.001$ m, the material parameters are constant as above. The plate is loaded uniformly and simply supported along the shanks (as indicated in Figure 3). We employ hard simply support, i.e. not only the displacement w but also the tangential component of the rotation ϕ_t is forced to zero.

Figure 4 displays the normalized value of the boundary layer function $\text{rot}(\phi)$ versus the distance from the boundary r . Clearly the boundary-layer equation contributes to the solution only in a very localized region near the plate boundary which has approximately the width of the plate thickness. Note that in the tangential direction the distribution of the boundary

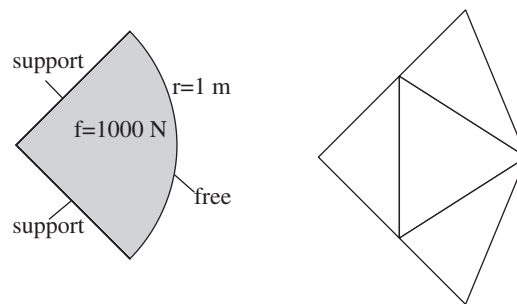


Figure 3. Model and initial mesh of the circular plate of Section 6.

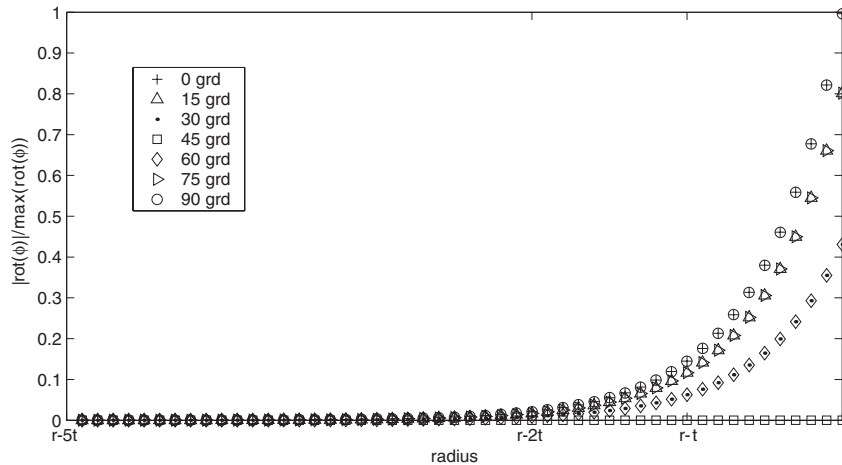


Figure 4. Analytically computed boundary layer function vs. distance for the example of Section 6.

layer is not uniform but symmetric, in particular in the symmetry plane (45 grd) its value is zero.

Our finite-element computation starts with a coarse mesh of four elements and obeys Algorithm (A); Figure 5 displays the generated meshes. The adaptive algorithm clearly resolves the boundary layer. We observe strong mesh-refinement along the free boundary because of high error contributions there. The generated meshes follow the distribution of the boundary-layer function, we get highly refined meshes at the outer sides and almost no refinement in the symmetry axis where $\text{rot}(\phi)=0$.

Because the solution is almost smooth the adaptive mesh refining is not expected to improve the solution quality substantially. But as displayed in Figure 6, the non-uniform meshes yield from the third refining step onwards the standard convergence rate of 1 whereas the uniform refinement converges only with a rate of $1/2$. This agrees well with the theoretical results of Pitkäranta and Suri [8], where because of boundary layers a reduced convergence rate of $1/2$ for uniform meshes (and very thin plates $t \rightarrow 0$) is predicted. Note that by adaptive refining techniques the error contribution of boundary layers may be reduced without the introduction of additional unknowns as proposed in Reference [8].

In conclusion, this example shows that the adaptive Algorithm (A) can overcome boundary layers and so significantly improves the accuracy of the finite-element approximations.

7. SHEET METAL WITH A HOLE

A rectangular sheet metal of Figure 7 loaded by two stamps of $0.2 \text{ m} \times 0.2 \text{ m}$ serves as a more practical example. The load of $f_w = 10^6 \text{ N}$ vanishes outside the marked region. On three sides (indicated with dashed lines in Figure 7) the steel plate is simply supported by hard support, $E = 2.1 \times 10^{12} \text{ N/m}^2$, $\nu = 0.3$, $t = 0.1 \text{ m}$.

By symmetry the coarse initial mesh consists of 17 finite elements with $N = 126$ degrees of freedom. Figure 8 displays the meshes generated by Algorithm (A). Since the load function

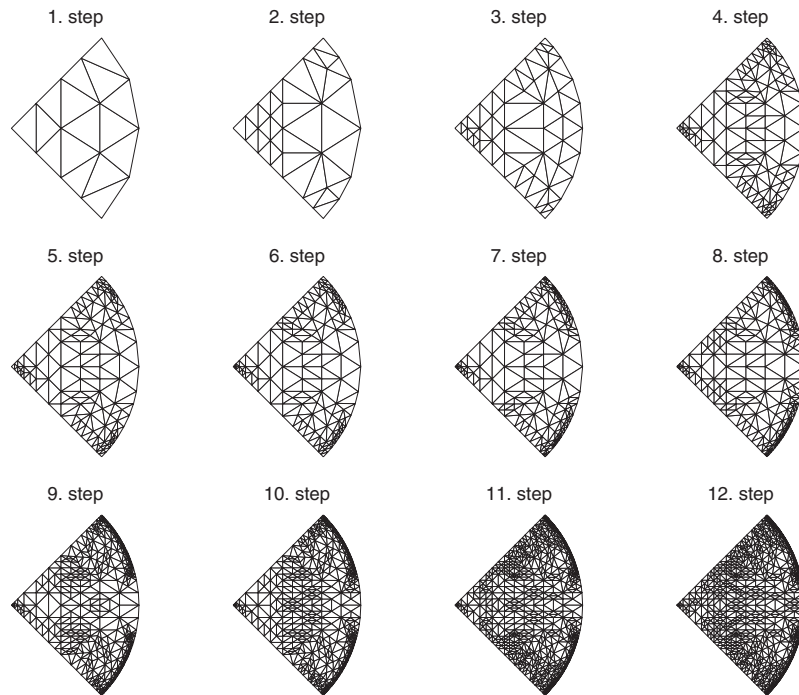


Figure 5. Adaptively generated meshes in the example of Section 6.

f_w is evaluated at the three Gauss points within T , f_w is reflected correctly only for meshes which are sufficiently fine around the load. If the mesh size is small compared to the stamp load (or at least decreased to a comparable size) the singularity is expected to be of minor influence.

The error estimate η_N is plotted in Figure 9 versus the number of degrees of freedom N in a log/log-scale and compared with uniform refinement technique. The vanishing influence of the load singularity is seen here by a high error-reduction in the beginning of the adaptive mesh refining and the standard convergence rate 1 for finer meshes (the geometry does not cause a non-smooth solution here).

Thus we deduced from Figure 9 that Algorithm (A) enables a significant reduction of computational effort, particularly, if it starts with very coarse initial meshes.

8. SINGULAR SOLUTION ON DOMAIN WITH RE-ENTERING CORNER

In our last example, an L-shaped plate $(-1,1)^2 \setminus [0,1]^2$ is clamped along the two edges of the domain which form the re-entering corner and is free at the remaining boundary. The (unknown) exact solution is expected to be singular near the origin at the re-entering corner even though the load is uniformly distributed; $t=0.01$ m, the material parameters are constant as in Section 3.1.

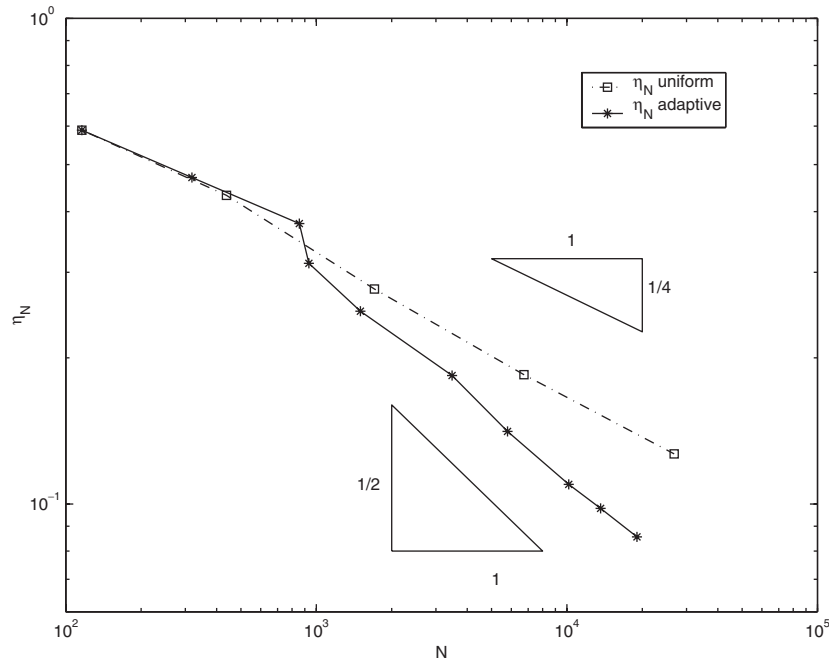


Figure 6. Convergence of error estimator (21) with uniform and adaptive refined meshes in the example of Section 6.

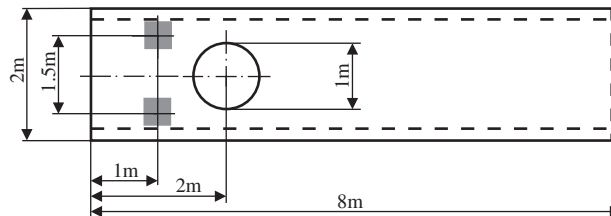


Figure 7. Sheet metal with hole and concentrated forces of Section 7.

We start our finite-element computation with a coarse mesh (Figure 10(a)) and refine uniformly but presumably sub-optimal. The convergence rate of error estimate η_N (Figure 11, dashed lines) is smaller than one.

This example typically illustrates the effect of adaptive designed, non-uniform meshes near singular points (typical meshes \mathcal{T}_4 , \mathcal{T}_7 after four and seven refinement steps, respectively, are shown in Figure 10). Employing the adaptive mesh-refining Algorithm (A) we obtain a significant reduction of error η_N up to the optimal convergence rate 1 (Figure 11, solid lines). This clearly supports that Algorithm (A) can overcome a loss of accuracy caused by corner singularities.

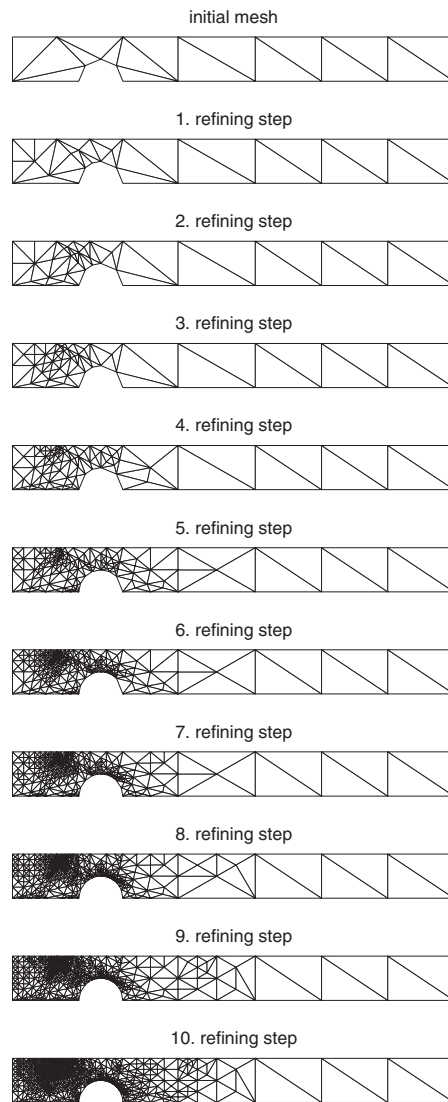


Figure 8. Adaptively generated meshes in the example of Section 7.

9. MATHEMATICAL JUSTIFICATION

The problem of Section 2, considered throughout the paper, differs from the formulation in References [1, 2] because of the bending energy term $(\varepsilon(\cdot); \mathbb{C}\varepsilon(\cdot))$ instead of $(\cdot; \cdot)$ and because of more general boundary conditions. This section is devoted to a brief review of the proof in Reference [2] and necessary modifications on the boundary. Hence, we suppose that neither Γ_D nor $\Gamma_N := \partial\Omega \setminus \Gamma_D$ are empty in this section.

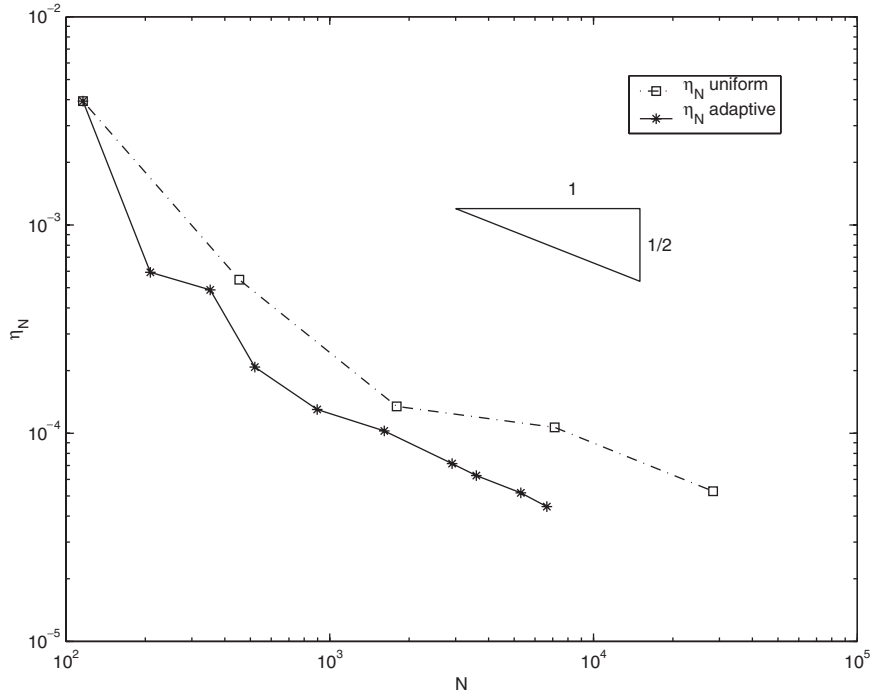


Figure 9. Convergence of error estimator (21) with uniform and adaptive refined meshes in the example of Section 7.

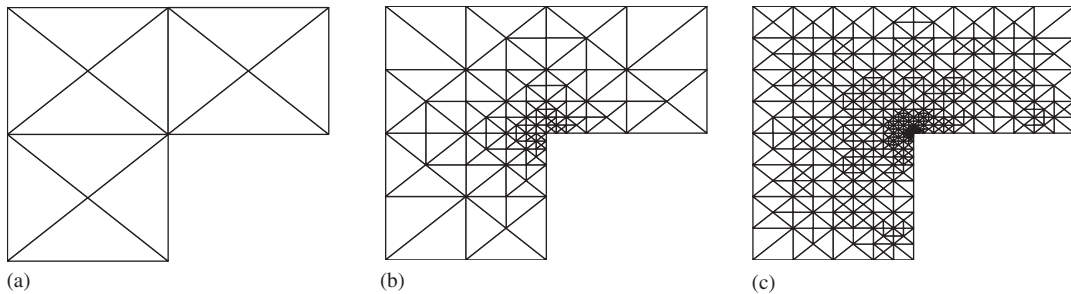


Figure 10. Finite-element meshes in the example of Section 8: (a) initial mesh $\mathcal{T}_0, N = 84$; (b) adapted mesh $\mathcal{T}_4, N = 1017$; and (c) adapted mesh $\mathcal{T}_7, N = 4293$.

In Step 1 we prove for η given in (21)–(22)

$$\|p - p_h\|_2 \lesssim \|\mathbb{C}\varepsilon(\phi - \phi_h)\|_2 + \|\nabla r - \nabla_{\mathcal{T}} r_h\|_{H_D^{-1}(\Omega)} + \eta \tag{28}$$

where \lesssim abbreviates an inequality up to a generic constant factor (which does not depend on $\mathbb{C}, h_{\mathcal{T}}, h_{\varepsilon}$ or t but may depend on the shape of the elements). The norm in $H_D^{-1}(\Omega)$, the

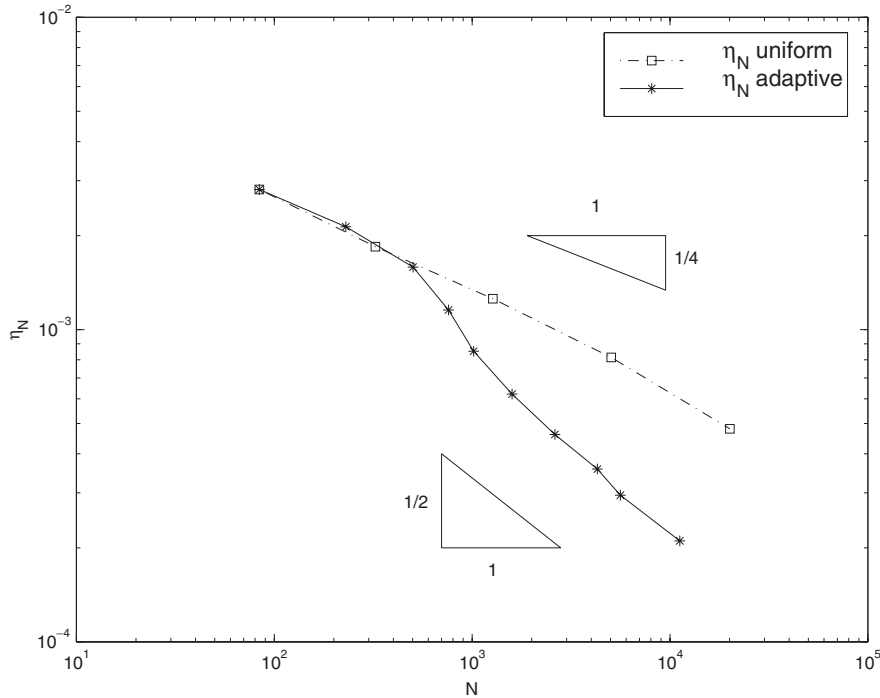


Figure 11. Convergence of error estimator (21) with uniform and adaptive refined meshes in the example of Section 8.

dual of $H_D^1(\Omega) := \{v \in H^1(\Omega) : v = 0 \text{ on } \Gamma_D\}$, is given by

$$\|\nabla r - \nabla_{\mathcal{T}} r_h\|_{H_D^{-1}(\Omega)} := \sup_{s \in H_D^1(\Omega) \setminus \{0\}} \frac{(s; \nabla r - \nabla_{\mathcal{T}} r_h)}{\|s\|_{1,2}} \tag{29}$$

An integration by parts as in Reference [2, Lemma 3.1] shows

$$\|\nabla r - \nabla_{\mathcal{T}} r_h\|_{H_D^{-1}(\Omega)} \lesssim \|r - r_h\|_2 + \|h_{\mathcal{E}}^{1/2}[r_h]\|_{L^2(\cup \mathcal{E})} \tag{30}$$

which is of higher order (if Ω is convex, it is of quadratic order). The discrete r_h was introduced in (12) and r is its continuous counterpart. Thus

$$\zeta = t^{-2}(\nabla w - \phi) = \nabla r + \text{Curl } p \tag{31}$$

for unique $r \in H_D^1(\Omega)$ and $p \in H_N^1(\Omega) := \{q \in H^1(\Omega) : q \text{ is constant on each connectivity component of } \Gamma_N\}$.

Sketch of the proof of (28)

We precede as in Reference [2, Lemma 3.3] and consider $\psi \in H_D^1(\Omega)^2$ with $p - p_h = \text{rot } \psi$ and $\|\psi\|_{1,2} \lesssim \|p - p_h\|_2$. (The existence of the solution and the bound follow from a solution of the Stokes equations with interchanged coefficients.) A \mathcal{T} -piecewise integration by parts

and a substitution of $\text{Curl}(p - p_h) = \zeta - \zeta_h - \nabla r + \nabla_{\mathcal{T}} r_h$ yields

$$\|p - p_h\|_2^2 = (\text{rot } \psi; p - p_h) = (\psi; \text{Curl}(p - p_h)) = (\psi; \zeta - \zeta_h - \nabla r + \nabla_{\mathcal{T}} r_h) \tag{32}$$

where we carefully notice that the boundary integrals vanish according to $\psi = 0$ on Γ_D and $\partial(p - p_h)/\partial s = 0$ and Γ_N . With (8), (14), and direct calculations, (32) is rewritten as

$$\begin{aligned} \|p - p_h\|_2^2 &= (\mathbb{C}\varepsilon(\phi_h); \varepsilon(\psi - \psi_h)) - (f_\phi + \zeta_h; \psi - \psi_h) - \int_{\Gamma_N} g_\phi(\psi - \psi_h) \, ds \\ &\quad + (\mathbb{C}\varepsilon(\phi - \phi_h); \varepsilon(\psi)) - (\psi; \nabla r - \nabla_{\mathcal{T}} r_h) \end{aligned} \tag{33}$$

Notice that $\mathbb{C}\varepsilon(\phi_h)$ is symmetric and so $(\mathbb{C}\varepsilon(\phi_h); \varepsilon(\psi - \psi_h)) = (\mathbb{C}\varepsilon(\phi_h); D\psi - D\psi_h)$. Thus, an elementwise integration by parts and the use of the Clément interpolation operator J for $\psi_h = J\psi$ with

$$\|h_{\mathcal{T}}^{-1}(\psi - \psi_h)\|_2 + \|h_{\mathcal{E}}^{-1/2}(\psi - \psi_h)\|_{2, \cup \mathcal{E}} + |\psi - \psi_h|_{1,2} \lesssim |\psi|_{1,2} \tag{34}$$

in (33) eventually leads to (28). Notice that the arising boundary terms vanish on Γ_D according to $\psi = 0$ there; on Γ_N we obtain $\int_{\Gamma_N} (g_\phi - \mathbb{C}\varepsilon(\phi_h)n)(\psi - \psi_h) \, ds$, while there arise the standard jump terms $\int_E [\mathbb{C}\varepsilon(\phi_h)]n_E(\psi - \psi_h) \, ds$ for each interior edge E . We omit the remaining details. \square

In Step 2 we prove

$$\begin{aligned} &\|\mathbb{C}^{1/2}\varepsilon(\phi - \phi_h)\|_2 + t\|\nabla(p - p_h)\|_2 + \|p - p_h\|_2 \\ &\lesssim \eta + \|\nabla r - \nabla_{\mathcal{T}} r_h\|_{H_D^{-1}(\Omega)} + \|\min\{t^{3/2}, th_{\mathcal{E}}^{1/2}\}[\partial r_h/\partial s]\|_{L^2(\cup \mathcal{E})} \end{aligned} \tag{35}$$

Well-established *a priori* and *a posteriori* error analysis of the finite-element discretization of the Laplace operator shows that $\|\nabla r - \nabla_{\mathcal{T}} r_h\|_2$ and $\|h_{\mathcal{E}}^{1/2}[\nabla r_h]\|_{L^2(\cup \mathcal{E})}$ are of linear convergence order [1, 2]. Hence $\|\min\{t^{3/2}, th_{\mathcal{E}}^{1/2}\}[\partial r_h/\partial s]\|_{L^2(\cup \mathcal{E})}$ is of higher order. Then we make use of $[\zeta_h]t_E = [\partial p/\partial n_E] + [\partial r/\partial t_E]$ and may regard $\|\min\{t^{3/2}, th_{\mathcal{E}}^{1/2}\}[\zeta_h t_E]\|_{L^2(\cup \mathcal{E})}$ as equal to $\|\min\{t^{3/2}, th_{\mathcal{E}}^{1/2}\}[\partial p_h/\partial n_E]\|_{L^2(\cup \mathcal{E})}$ up to higher-order terms. The advantage of having $\|\min\{t^{3/2}, th_{\mathcal{E}}^{1/2}\}[\zeta_h t_E]\|_{L^2(\cup \mathcal{E})}$ in (22) is its direct computability (the computation of p_h requires little extra efforts).

Sketch of the proof of (35)

Since $\partial(p - p_h)/\partial s = 0$ (almost everywhere) on Γ_N and $w - t^2 r = 0$ on Γ_D ,

$$(\text{Curl}(p - p_h); \phi + t^2 \text{Curl } p) = (\text{Curl}(p - p_h); \nabla w - t^2 \nabla r) = 0$$

Similarly (since $\text{Curl } \mathcal{S}_N^1(\mathcal{T})$ is L^2 -orthogonal to $\nabla_{\mathcal{T}} \mathcal{S}_D^{1,NC}(\mathcal{T})$), for any $q_h \in \mathcal{S}_N^1(\mathcal{T})$,

$$(\text{Curl } q_h; \phi_h + t^2 \text{Curl } p_h) = (\text{Curl } q_h; P_0 \phi_h + t^2 \text{Curl } p_h) = (\text{Curl } q_h; \nabla_{\mathcal{T}} w_h - t^2 \nabla_{\mathcal{T}} r_h) = 0$$

The preceding two identities yield

$$t^2 \|\text{Curl}(p - p_h)\|_2^2 = -(\text{Curl}(p - p_h); \phi - \phi_h) - (\text{Curl}(p - p_h - q_h); \phi_h + t^2 \text{Curl } p_h)$$

Adding $\|\mathbb{C}^{1/2}\varepsilon(\phi - \phi_h)\|_2^2 = a(\phi - \phi_h; \phi - \phi_h)$ and rewriting the term

$$(\zeta - \zeta_h; \phi - \phi_h) = (\text{Curl}(p - p_h); \phi - \phi_h) + (\nabla r - \nabla_{\mathcal{T}} r_h; \phi - \phi_h)$$

with (5) we deduce

$$\begin{aligned} &\|\mathbb{C}^{1/2}\varepsilon(\phi - \phi_h)\|_2^2 + t^2\|\text{Curl}(p - p_h)\|_2^2 = a(\phi - \phi_h; \phi - \phi_h) \\ &\quad + b(\phi - \phi_h, 0; \zeta - \zeta_h) + (\phi - \phi_h; \nabla r - \nabla_{\mathcal{T}} r_h) - (\text{Curl}(p - p_h - q_h); \phi_h + t^2 \text{Curl } p_h) \end{aligned}$$

According to (8) and (10) we obtain, for each $\psi_h \in \mathcal{S}_D^1(\mathcal{T})$,

$$a(\phi - \phi_h; \psi_h) + b(\psi_h, 0; \zeta - \zeta_h) = 0$$

Hence, with further rewriting in terms of the bilinear forms, we obtain

$$\begin{aligned} &\|\mathbb{C}^{1/2}\varepsilon(\phi - \phi_h)\|_2^2 + t^2\|\text{Curl}(p - p_h)\|_2^2 \\ &= a(\phi - \phi_h; \phi - \phi_h - \psi_h) + b(\phi - \phi_h - \psi_h, 0; \zeta - \zeta_h) \\ &\quad + (\phi - \phi_h; \nabla r - \nabla_{\mathcal{T}} r_h) - (\text{Curl}(p - p_h - q_h); \phi_h + t^2 \text{Curl } p_h) \\ &= F(\phi - \phi_h - \psi_h, 0) - (\mathbb{C}\varepsilon(\phi_h); \varepsilon(\phi - \phi_h - \psi_h)) + (\zeta_h; \phi - \phi_h - \psi_h) \\ &\quad - (\text{Curl}(p - p_h - q_h); \phi_h + t^2 \text{Curl } p_h) + (\phi - \phi_h; \nabla r - \nabla_{\mathcal{T}} r_h) \end{aligned}$$

An elementwise integration by parts in $(\mathbb{C}\varepsilon(\phi_h); D(\phi - \phi_h - \psi_h))$ and in $(\text{Curl}(p - p_h - q_h); \phi + t^2 \text{Curl } p_h)$ results in

$$\begin{aligned} &\|\mathbb{C}^{1/2}\varepsilon(\phi - \phi_h)\|_2^2 + t^2\|\text{Curl}(p - p_h)\|_2^2 \\ &= (\zeta_h + \text{div}_{\mathcal{T}} \mathbb{C}\varepsilon(\phi_h) + f_\phi; \phi - \phi_h - \psi_h) \\ &\quad - \int_{\cup \mathcal{E}} [\mathbb{C}\varepsilon(\phi_h)n_{\mathcal{E}}](\phi - \phi_h - \psi_h) \, ds - (\text{rot } \phi_h; p - p_h - q_h) \\ &\quad + \int_{\cup \mathcal{E}} t^2[\partial p_h/\partial n_{\mathcal{E}}](p - p_h - q_h) \, ds + (\phi - \phi_h; \nabla r - \nabla_{\mathcal{T}} r_h) \end{aligned}$$

where $[\mathbb{C}\varepsilon(\phi_h)n_E]$ denotes the jump of $\mathbb{C}\varepsilon(\phi_h)$ over an interior edge E in its normal direction, $[\mathbb{C}\varepsilon(\phi_h)n_E] := 0$ for E on Γ_D (as $\phi - \phi_h - \psi_h = 0$ there), and $[\mathbb{C}\varepsilon(\phi_h)n_E] := g_\phi - \mathbb{C}\varepsilon(\phi)n$ on Γ_N ; similarly, $p - p_h - q_h$ vanishes on Γ_D (as $p - p_h$ is constant on each connectivity component of Γ_D and q_h can eliminate this constant) and so $[\partial p_h/\partial n_E] := 0$ on Γ_D , equals $\partial p_h/\partial n$ on Γ_N , and denotes the jump of the piecewise constants ∇p_h across interior element edges in their normal components.

The proof is finished with standard approximation arguments (cf. (34)) as in Step 1. Estimate (35) involves the minimum of $t^{3/2}$ and $th_{\mathcal{E}}^{1/2}$. The first option follows with the above arguments, the second follows with Step 1. Indeed, a closer look at the trace inequalities reveals that we can use the estimates for $\|p - p_h\|_2 + t\|\text{Curl}(p - p_h)\|_2$ (even locally) to absorb $t^{1/2}\|p - p_h - q_h\|_2$. We refer to Reference [2, Lemma 3.3] for the rather technical

details and omit them here as they are not affected by different boundary conditions or the modification on the operator $\mathbb{C}\varepsilon$. \square

In Step 3 we recall an argument from Reference [2] that shows that $\|\phi_h - P_0\phi_h\|_2 = \|\phi_h - \nabla w_h + t^2\zeta_h\|_2$ dominates the error $\|\nabla w - \nabla_{\mathcal{T}}w_h\|_2$ in the vertical displacements, namely,

$$\|\nabla w - \nabla_{\mathcal{T}}w_h\|_2 - \|\phi_h - P_0\phi_h\|_2 \leq \|\phi - \phi_h\|_2 + r^2\|\text{Curl}(p - p_h)\|_2 + t^2\|\nabla r - \nabla_{\mathcal{T}}r_h\|_2 \quad (36)$$

Sketch of the proof of (36)

The proof of (36) is by the triangle inequality for the identity

$$(\nabla w - \nabla_{\mathcal{T}}w_h) - (\phi_h - P_0\phi_h) = \phi - \phi_h + t^2(\nabla r - \nabla_{\mathcal{T}}r_h + \text{Curl } p - \text{Curl } p_h) \quad \square$$

The dominance of $\|\phi_h - P_0\phi_h\|_2$ from (36) gives the resulting estimate

$$\|\nabla w - \nabla_{\mathcal{T}}w_h\|_2 \leq \eta + \|\phi - \phi_h\|_2 + t^2\|\nabla r - \nabla_{\mathcal{T}}r_h\|_2 \quad (37)$$

which follows from an L^2 -estimate (cf. References [1] and [2, Proposition 3.6]) as $\|\phi - \phi_h\|_2 \leq \|\mathbb{C}^{1/2}\varepsilon(\phi - \phi_h)\|_2$ and $t^2\|\nabla r - \nabla_{\mathcal{T}}r_h\|_2 = O(t^2h)$ is of higher order.

In summary, we have sketched the proof of the reliability of η .

Theorem 9.1

Estimator (21)–(22) is reliable in the sense that

$$\begin{aligned} & \|\mathbb{C}^{1/2}\varepsilon(\phi - \phi_h)\|_2 + t\|\nabla(p - p_h)\|_2 + \|p - p_h\|_2 + \|\nabla w - \nabla_{\mathcal{T}}w_h\|_2 \\ & \lesssim \eta + \|\nabla r - \nabla_{\mathcal{T}}r_h\|_{H_0^{-1}(\Omega)} + t^2\|\nabla r - \nabla_{\mathcal{T}}r_h\|_2 + \|\phi - \phi_h\|_2 \end{aligned} \quad (38)$$

Remark 9.1

The interpretation is that, besides η , the upper bound consists of higher-order terms. The point is that (38) involves exclusively (h, t) -independent constants behind the notation \lesssim .

Remark 9.2

Estimate (38) is efficient in the sense that the converse inequality holds even in a local form up to higher-order terms which depend on the smoothness of the given data. We refer to Reference [2, Theorem 4.8] for details in a simplified context.

ACKNOWLEDGEMENTS

The first author (KW) thankfully acknowledges partial support by the German Research Foundation (DFG) within the Graduiertenkolleg ‘Effiziente Algorithmen und Mehrskalenmethoden’.

REFERENCES

1. Arnold D, Falk R. A uniformly accurate finite element method for the Reissner–Mindlin plate model. *SIAM Journal on Numerical Analysis* 1989; **26**:1276–1290.
2. Carstensen C. Residual-based *a posteriori* error estimate for a nonconforming Reissner–Mindlin plate finite element. *SIAM Journal on Numerical Analysis* 2002; **39**(6):2034–2044.
3. Carstensen C, Weinberg K. Calculating the energy-norm fem-error for Reissner–Mindlin plates without known reference solution. *Computational Mechanics* 2000; **26**:566–570.

4. Carstensen C, Weinberg K. Adaptive mixed finite element method for Reissner–Mindlin plate. *Computer Methods in Applied Mechanics and Engineering* 2001; **190**(51–52):6895–6908.
5. Brenner S, Scott L. The mathematical theory of finite element methods. *Texts in Applied Mathematics*, vol. 15. Springer, New York, 1994.
6. Verfürth R. *A Review of A Posteriori Error Estimation and Adaptive Mesh-refinement Techniques*. Wiley: New York, Teubner: Leipzig, 1996.
7. Nosier A, Yavari A, Sarkani S. Study of edge-zone equation of Mindlin–Reissner plate theory. *Journal of Engineering Mechanics* (ASCE) 2000; **126**(6):647–651.
8. Pitkäranta J, Suri M. Upper and lower error bounds for plate-bending finite elements. *Numerische Mathematik* 2000; **84**:611–648.